AIAA SciTech Forum
9 - 13 January 2017, Grapevine, Texas
55th AIAA Aerospace Sciences Meeting

10.2514/6.2017-1006

Large eddy simulation of surging airfoils with moderate to large streamwise oscillations

A. Kocher*, R. Cummings†, S. Tran‡, and O. Sahni§
Rensselaer Polytechnic Institute, Troy, NY, 12180, USA

A large eddy simulation (LES) based numerical investigation is carried out for flow over two surging airfoils with moderate to large streamwise oscillations. In each case, the airfoil is subjected to a sinusoidal surging motion with streamwise oscillation at a fixed angle of attack. The amplitude of the sinusoidal oscillation is varied within a moderate range as well as in the high range. The amplitude of oscillation is characterized by the advance ratio, which is defined as the ratio of the maximum relative velocity in excess to the mean relative velocity (or mean free-stream velocity) to the mean relative velocity. The relative velocity is defined between the airfoil and ambient fluid. For the moderate range, NACA 0018 airfoil at a mean Reynolds number of 300,000 and 4° angle of attack is considered. Two advance ratios of 0.34 and 0.51 are considered to match with the experiments of Strangfeld *et al.*[1] For the high range, NACA 0012 airfoil at a mean Reynolds number of 40,000 and 6° angle of attack is considered at three advance ratios of 0.8, 1.0 and 1.2 to match with the experiments of Granlund *et al.*[2] Note that the highest advance ratio case involves the reversed flow condition, where in a part of the surging cycle the relative flow becomes negative or is from the geometric trailing end of the airfoil to the leading end.

Lift force is compared between the experiments and simulations. Overall a good agreement is obtained for the lift force in all cases. Additionally, for all cases flowfields from simulations are examined at different phases of the surge cycle. For the moderate advance ratio cases, a similar flow pattern is observed between the two advance ratios and no distinct vortex is shed from the airfoil. On the other hand, in all three high advance ratio cases a distinct vortex is shed near the (geometric) leading edge on the suction or upper side. This prominent leading-edge vortex is shed as the minimum velocity is reached in the surging cycle and advects downstream (in the horizontal direction) by roughly the mean free-stream velocity. The relative position of the shed vortex (with respect to the airfoil) varies significantly between the three high advance ratio cases; it crosses the leading edge before sweeping over the airfoil in the case with the highest advance ratio of 1.2 (i.e., in the case with the reverse flow regime).

I. Introduction

In a forward rotorcraft flight, each section of a rotorcraft blade is subjected to a cyclic relative velocity due to the forward motion of the rotorcraft along with the rotational motion of the blade. The extent or amplitude of the oscillations in the relative velocity is determined by the advance ratio, which for the rotorcraft is defined as the ratio of the forward velocity to the rotational velocity at the blade tip. Local rotational speed is used when considering a section of the blade, which undergoes a cyclic surging motion in a forward flight. Additionally, a cyclic pitching motion is typically applied as the blade rotates along the azimuth. A plunging motion may also be present (e.g., due to unsteady blade deformation or flapping). Therefore, the relative motion is typically decomposed into pitch, plunge, and surge components.

Such a relative motion leads to large changes in the lift and drag forces experienced by the blades in each revolution. For example, a high lift is generated as the blade advances and small to no lift is generated as

*M.S. Student, AIAA Student Member, Department of Mechanical, Aerospace and Nuclear Engineering, RPI
†Postdoctoral Research Associate, Scientific Computational Research Center, RPI
‡Ph.D. Student, Department of Mechanical, Aerospace and Nuclear Engineering, RPI
§Assistant Professor, AIAA Senior Member, Department of Mechanical, Aerospace and Nuclear Engineering, RPI

the blade retreats. Further, under a high forward speed a large rate of change, or a sudden change, in forces and moments is also experienced due to a drastic change in the flow behavior around the blades. In such cases, the flow around the blades involves complex flow phenomena such as dynamic stall and reverse flow.

A number of experimental and numerical studies have been performed to understand the flow behavior around rotorcraft blades in a forward flight. Some of the recent studies have been carried out by conducting experiments in a quasi-3D environment in which a blade model is subjected to an unsteady free-stream or a cyclic surging and/or pitching motion. Strangfeld *et al.*[1] investigated flow over an airfoil subjected to an unsteady free-stream with a moderate level of oscillations. While Granlund *et al.*[2] considered the effect of large streamwise oscillations imposed on a blade model including a reverse flow regime through water tunnel experiments. Greenblatt *et al.*[3] studied the effects of an oscillating free-stream velocity and cyclic pitching on an airfoil section through experiments. Numerical simulations have also been used as an effective way to understand such complex flows. Numerical investigations on a quasi-3D model include that of Visbal[4] in which a high-order finite difference based large eddy simulation (LES) was employed. Hodara *et al.*[5] investigated a pitching airfoil in a constant reverse flow (leading to a reverse dynamic stall) through a joint wind tunnel testing and numerical simulation based on a hybrid Reynolds-averaged Navier-Stokes (RANS)-LES approach. Other studies have investigated flow over the entire rotor in a forward flight through experimental testing (e.g., Norman *et al.*[6]) and numerical simulations (e.g., Potsdam *et al.*[7]).

In this study, finite element based LES is used to study flow over two airfoils undergoing surging motion (only). LES is an attractive methodology since it is tractable from a computational viewpoint as well as sufficiently accurate. Current LES approach is based on the finite element (FE) method and uses a combined subgrid-scale model which employs the residual-based variational multiscale (RBVMS) model along with the dynamic Smagorinsky model.[8–10] The dynamic procedure is based on a localized version of the variational Germano identity (VGI).[8,9] An arbitrary Lagrangian Eulerian (ALE) description is used to account for the relative motion of the airfoil.[11] The ease with which the FE method can be applied on unstructured meshes makes it a useful option for investigating many challenging problems of interest. Furthermore, the adaptive meshing,[12–14] high-order,[15,16] and parallelization[17–19] capabilities of the FE method can significantly increase the computational efficiency.

Two sets of cases are considered. In each set, the airfoil is subjected to a sinusoidal surging motion with streamwise oscillation at a fixed angle of attack and under a constant free-stream velocity. In one set, the amplitude of the oscillation is varied within a moderate range, while a high range is considered in the other set. The amplitude of oscillation is characterized by the advance ratio of the airfoil section, which is currently defined as the ratio of the maximum relative velocity in excess to the free-stream velocity to the free-stream velocity. The relative velocity is defined between the airfoil and ambient fluid. For the moderate range, NACA 0018 airfoil at a mean Reynolds number of 300,000 and 4° angle of attack is considered. Two advance ratios of 0.34 and 0.51 are considered to match with the experiments of Strangfeld *et al.*[1] For the high range, NACA 0012 airfoil at a mean Reynolds number of 40,000 and 6° angle of attack is considered at three advance ratios of 0.8, 1.0 and 1.2 to match with the experiments of Granlund *et al.*[2] Note that the highest advance ratio case involves the reversed flow condition, where in a part of the surging cycle the relative flow becomes negative or is from the geometric trailing end of the airfoil to the leading end. For each set, lift forces are compared between the experiments and simulations. Additionally, flowfields at different phases of the surge cycle are examined from simulations.

The organization of this paper is as follows. The current LES methodology is presented in Section II, where the combined model formulation and dynamic procedure are discussed in Sections II.A and II.B, respectively. Results and discussion are provided in Section III, where we first describe the problem setup and discretization in Section III.A. LES results for the moderate advance ratio cases are discussed in Section III.B, for which force comparison and flowfields are presented in Sections III.B.1 and III.B.2, respectively. Similarly, results for the high advance ratio cases are presented in Section III.C with force comparison in Section III.C.1 and flowfields in Section III.C.2. Closing remarks are discussed in Section IV.

II. Dynamic Large Eddy Simulations

A dynamic LES methodology is currently employed. It uses a combined subgrid-scale model which is based on the residual-based variational multiscale (RBVMS) model along with the dynamic Smagorinsky model.[8–10] The dynamic procedure is local in nature and is based on a localized version of the variational Germano identity.[8,9] In this local procedure, Lagrangian averaging along fluid pathtubes is applied to make

it robust. Further, an arbitrary Lagrangian Eulerian (ALE) description is used to account for the deforming mesh due to the relative motion of the airfoil.[11]

II.A. Combined Model Formulation

This work uses the incompressible Navier Stokes equations in the arbitrary Lagrangian Eulerian (ALE) description. The strong form of the equations is given as

$$\begin{aligned} &u_{k,k} = 0 \\ &u_{i,t} + (u_j - u_j^m)u_{i,j} = -p_{,i} + \tau_{ij,j}^{\nu} + f_i \end{aligned} \tag{1}$$

where u_i is the velocity vector, u_i^m is the mesh velocity vector, p is the pressure (scaled by the constant density), $\tau_{ij}^{\nu} = 2\nu S_{ij}$ is the symmetric (Newtonian) viscous stress tensor (scaled by the density), ν is the kinematic viscosity, $S_{ij} = 0.5(u_{i,j} + u_{j,i})$ is the strain-rate tensor, and f_i is the body force vector (per unit mass). Note that Einstein summation notation is used.

The weak form is stated as follows: find $\mathbf{u} \in \boldsymbol{\mathcal{S}}$ and $p \in \mathcal{P}$ such that

$$\begin{aligned} B(\{w_i, q\}, \{u_i, p\}; u_l^m) = &\int_{\Omega} [w_i(u_{i,t} + u_i u_{j,j}^m) + w_{i,j}(-u_i(u_j - u_j^m) + \tau_{ij}^{\nu} - p\delta_{ij}) - q_{,k}u_k]\, d\Omega \\ &+ \int_{\Gamma_h} [w_i(u_i(u_j - u_j^m) - \tau_{ij}^{\nu} + p\delta_{ij})n_j + qu_k n_k]\, d\Gamma_h \\ &= \int_{\Omega} w_i f_i d\Omega \end{aligned} \tag{2}$$

for all $\mathbf{w} \in \boldsymbol{\mathcal{W}}$ and $q \in \mathcal{P}$. $\boldsymbol{\mathcal{S}}$ and $\mathcal{P}$ are suitable trial/solution spaces and $\boldsymbol{\mathcal{W}}$ is the test/weight space. $\mathbf{w}$ and q are the weight functions for the velocity and pressure variables, respectively. Ω is the spatial domain and Γ_h is the portion of the domain boundary with Neumann or natural boundary conditions.

The above weak form can be written concisely as: find $\boldsymbol{U} \in \boldsymbol{\mathcal{U}}$ such that

$$B(\boldsymbol{W}, \boldsymbol{U}; u_l^m) = (\boldsymbol{W}, \boldsymbol{F}) \tag{3}$$

for all $\boldsymbol{W} = [\mathbf{w}, q]^T \in \boldsymbol{\mathcal{V}}$. $\boldsymbol{U} = [\mathbf{u}, p]^T$ is the vector of unknown solution variables and $\boldsymbol{F} = [\mathbf{f}, 0]^T$ is the source vector. The solution and weight spaces are: $\boldsymbol{\mathcal{U}} = \{\boldsymbol{U} = [\mathbf{u}, q]^T | \mathbf{u} \in \boldsymbol{\mathcal{S}}; p \in \mathcal{P}\}$ and $\boldsymbol{\mathcal{V}} = \{\boldsymbol{W} = [\mathbf{w}, q]^T | \mathbf{w} \in \boldsymbol{\mathcal{W}}; q \in \mathcal{P}\}$, respectively.

Throughout this text $B(\cdot, \cdot)$ is used to represent the semi-linear form that is linear in its first argument and $(\cdot, \cdot)$ is used to denote the L_2 inner product. $B(\boldsymbol{W}, \boldsymbol{U}; u_l^m)$ is split into bilinear and semi-linear terms as shown below.

$$B(\boldsymbol{W}, \boldsymbol{U}; u_l^m) = B_1(\boldsymbol{W}, \boldsymbol{U}; u_l^m) + B_2(\boldsymbol{W}, \boldsymbol{U}) = (\boldsymbol{W}, \boldsymbol{F}) \tag{4}$$

where $B_1(\boldsymbol{W}, \boldsymbol{U}; u_l^m)$ contains the bilinear terms and $B_2(\boldsymbol{W}, \boldsymbol{U})$ is the semi-linear term. These are defined as

$$\begin{aligned} B_1(\boldsymbol{W}, \boldsymbol{U}; u_l^m) = &\int_{\Omega} [w_i(u_{i,t} + u_i u_{j,j}^m) + w_{i,j}(u_i u_j^m + \tau_{ij}^{\nu} - p\delta_{ij}) - q_{,k}u_k]\, d\Omega \\ &+ \int_{\Gamma_h} [w_i(-u_i u_j^m - \tau_{ij}^{\nu} + p\delta_{ij})n_j + qu_k n_k]\, d\Gamma_h \end{aligned} \tag{5}$$

$$B_2(\boldsymbol{W}, \boldsymbol{U}) = -\int_{\Omega} w_{i,j} u_i u_j d\Omega + \int_{\Gamma_h} w_i u_i u_j n_j d\Gamma_h \tag{6}$$

The Galerkin weak form is obtained by considering the finite-dimensional or discrete solution spaces $\boldsymbol{\mathcal{S}}^h \subset \boldsymbol{\mathcal{S}}$ and $\mathcal{P}^h \subset \mathcal{P}$ and the weight space $\boldsymbol{\mathcal{W}}^h \subset \boldsymbol{\mathcal{W}}$, where the superscript h is used as a mesh parameter to denote discretized spaces and variables in a finite element context. Using these spaces, $\boldsymbol{\mathcal{U}}^h = \{\boldsymbol{U}^h = [\mathbf{u}^h, p^h]^T | \mathbf{u}^h \in \boldsymbol{\mathcal{S}}^h; p^h \in \mathcal{P}^h\}$ and $\boldsymbol{\mathcal{V}}^h = \{\boldsymbol{W}^h = [\mathbf{w}^h, q^h]^T | \mathbf{w}^h \in \boldsymbol{\mathcal{W}}^h; q^h \in \mathcal{P}^h\}$ are defined. The Galerkin weak form is then stated concisely as: find $\boldsymbol{U}^h \in \boldsymbol{\mathcal{U}}^h$ such that

$$B(\boldsymbol{W}^h, \boldsymbol{U}^h) = (\boldsymbol{W}^h, \boldsymbol{F}) \tag{7}$$

for all $\boldsymbol{W}^h \in \boldsymbol{\mathcal{V}}^h$. Note for brevity we have dropped u_l^m term. The Galerkin weak formulation corresponds to a method for direct numerical simulation since no modeling is employed. However, when the finite-dimensional spaces are incapable of representing the fine/small scales, the Galerkin formulation yields an inaccurate solution. A model term is added to overcome this difficulty, e.g., as done in the residual-based variational multiscale (RBVMS) formulation.

In RBVMS, a set of model terms is added to the Galerkin weak that results in the following variational formulation: find $\boldsymbol{U}^h \in \boldsymbol{\mathcal{U}}^h$ such that

$$B(\boldsymbol{W}^h, \boldsymbol{U}^h) + M_{rbvms}(\boldsymbol{W}^h, \boldsymbol{U}^h) = (\boldsymbol{W}^h, \boldsymbol{F}) \tag{8}$$

for all $\boldsymbol{W}^h \in \boldsymbol{\mathcal{V}}^h$. M_{rbvms} represents the set of model terms due to the RBVMS approach.

A scale separation is used to decompose the solution and weight spaces as $\boldsymbol{\mathcal{S}} = \boldsymbol{\mathcal{S}}^h \oplus \boldsymbol{\mathcal{S}}'$ and $\mathcal{P} = \mathcal{P}^h \oplus \mathcal{P}'$, and $\boldsymbol{\mathcal{W}} = \boldsymbol{\mathcal{W}}^h \oplus \boldsymbol{\mathcal{W}}'$, respectively. Thus, the solution and weight functions are decomposed as $u_i = u_i^h + u_i'$ and $p = p^h + p'$ or $\boldsymbol{U} = \boldsymbol{U}^h + \boldsymbol{U}'$, and $w_i = w_i^h + w_i'$ and $q = q^h + q'$ or $\boldsymbol{W} = \boldsymbol{W}^h + \boldsymbol{W}'$, respectively. Note that coarse-scale or resolved quantities are denoted by $(\cdot)^h$ and fine-scale or unresolved quantities by $(\cdot)'$. The coarse-scale quantities are resolved by the grid whereas the effects of the fine scales on the coarse scales are modeled. In RBVMS, the fine scales are modeled as a function of the strong-form residual due to the coarse-scale solution. This is represented abstractly as $\boldsymbol{U}' = \mathcal{F}(\boldsymbol{R}(\boldsymbol{U}^h); \boldsymbol{U}^h)$, where $\boldsymbol{R}(\cdot) = [\boldsymbol{R}^m(\cdot), R^c(\cdot)]^T$ is the strong-form residual of the equations with $\boldsymbol{R}^m(\cdot)$ (or $R_i^m(\cdot)$) and $R^c(\cdot)$ as those of the momentum and continuity equations, respectively. Specifically, the fine-scale quantities are modeled as $u_i' \approx -\tau_M R_i^m(u_k^h, p^h; u_l^m)$ and $p' \approx -\tau_C R^c(u_k^h)$, where τ_C and τ_M are stabilization parameters (e.g., see details in Tran and Sahni[9,10]). This provides a closure to the coarse-scale problem as it involves coarse-scale solution as the only unknown. This is why $M_{rbvms}(\boldsymbol{W}^h, \boldsymbol{U}^h)$ is written only in terms of the unknown coarse-scale solution $\boldsymbol{U}^h$. In summary, $M_{rbvms}(\boldsymbol{W}^h, \boldsymbol{U}^h)$ is as follows

$$\begin{aligned} M_{rbvms}(\boldsymbol{W}^h, \boldsymbol{U}^h) = \sum_e \int_{\Omega_e^h} [& \underbrace{-(w_i^h u_{j,j}^m + w_{i,j}^h u_j^m)\tau_M R_i^m(u_k^h, p^h; u_l^m)}_{M_{rbvms}^{ALE}(\boldsymbol{W}^h, \boldsymbol{U}^h)} \\ & + \underbrace{q_{,i}^h \tau_M R_i^m(u_k^h, p^h; u_l^m)}_{M_{rbvms}^{cont}(\boldsymbol{W}^h, \boldsymbol{U}^h)} + \underbrace{w_{i,j}^h \tau_C R^c(u_k^h)\delta_{ij}}_{M_{rbvms}^{P}(\boldsymbol{W}^h, \boldsymbol{U}^h)} \\ & + \underbrace{w_{i,j}^h \left(u_i^h \tau_M R_j^m(u_k^h, p^h; u_l^m) + \tau_M R_i^m(u_k^h, p^h; u_l^m) u_j^h\right)}_{M_{rbvms}^{C}(\boldsymbol{W}^h, \boldsymbol{U}^h)} \\ & \underbrace{-w_{i,j}^h \tau_M R_i^m(u_k^h, p^h; u_l^m)\tau_M R_j^m(u_k^h, p^h)}_{M_{rbvms}^{R}(\boldsymbol{W}^h, \boldsymbol{U}^h)}] d\Omega_e^h \end{aligned} \tag{9}$$

Note that all model terms are written in terms of the resolved scales within each element (where e denotes an element and contributions from all elements are summed). The last model term is used to represent the Reynolds stresses (i.e., M_{rbvms}^R) while the terms prior to it are used to represent the cross-stress terms (i.e., M_{rbvms}^C).

In previous studies,[9,20] it was found that the RBVMS model provides a good approximation for the turbulent dissipation due to the cross stresses but the dissipation due to the Reynolds stresses is underpredicted and turns out to be insufficient. Therefore, a combined subgrid-scale model was employed which uses the RBVMS model for the cross-stress terms and the dynamic Smagorinsky eddy viscosity model for the Reynolds stress terms. This was done in both a spectral code[20] and a finite element code.[8,9] The combined subgrid-scale model is defined as

$$B(\boldsymbol{W}^h, \boldsymbol{U}^h) + M_{comb}(\boldsymbol{W}^h, \boldsymbol{U}^h; C_S, h) = (\boldsymbol{W}^h, \boldsymbol{F}) \tag{10}$$

where

$$\begin{aligned} M_{comb}(\boldsymbol{W}^h, \boldsymbol{U}^h; C_S, h) =& M^{ALE}_{rbvms}(\boldsymbol{W}^h, \boldsymbol{U}^h) + M^{cont}_{rbvms}(\boldsymbol{W}^h, \boldsymbol{U}^h) + M^{P}_{rbvms}(\boldsymbol{W}^h, \boldsymbol{U}^h) \\ &+ M^{C}_{rbvms}(\boldsymbol{W}^h, \boldsymbol{U}^h) + (1-\gamma) M^{R}_{rbvms}(\boldsymbol{W}^h, \boldsymbol{U}^h) \\ &+ \gamma M^{R}_{smag}(\boldsymbol{W}^h, \boldsymbol{U}^h; C_S, h) \end{aligned} \tag{11}$$

$$M^{R}_{smag}(\boldsymbol{W}^h, \boldsymbol{U}^h; C_S, h) = \int_\Omega w^h_{i,j} 2 \nu_t S^h_{ij} d\Omega = \int_\Omega w^h_{i,j} 2 \underbrace{(C_S h)^2 |S^h|}_{\nu_t} S^h_{ij} d\Omega \tag{12}$$

where ν_t is the eddy viscosity, $|S^h|$ is the norm of the strain-rate tensor (i.e., $|S^h| = \sqrt{2\boldsymbol{S}^h : \boldsymbol{S}^h} = \sqrt{2 S^h_{ij} S^h_{ij}}$), h is the local mesh size, and C_S is the Smagorinsky parameter. The parameter γ is set to be either 0 or 1 in order to control which model is used for the Reynolds stresses. Note that $\gamma = 0$ results in the original RBVMS model and $\gamma = 1$ results in the combined subgrid-scale model. The Smagorinsky parameter is computed dynamically in a local fashion as discussed below.

II.B. Dynamic Procedure

To dynamically compute the Smagorinsky parameter in a local fashion, we follow the localized version of the variational Germano identity (VGI) developed by Tran *et al.*[8,9] In this local procedure, Lagrangian averaging along fluid pathtubes is applied to make it robust. The dynamic local procedure and the associated approximations are summarized in this section.

II.B.1. Local Variational Germano Identity

The VGI involves comparing the variational form (including the model terms) between different levels of the discretization such that they are nested. In the localized version of the VGI, a set of nested spaces are constructed by using a series of coarser second-level grids along with the primary or original grid. We refer to the primary grid as the h-grid and any grid in the series of second-level grids as the H-level grid. Each H-level grid is chosen such that it is associated with an interior node in the primary grid. This is done such that each H-grid is identical to the h-grid except that the given node k in the h-grid is coarsened or removed resulting in a nested H-level grid for node k, which we refer to as the H_k-grid. Note that each H_k-grid involves local coarsening around a given node k while the remainder of the mesh remains the same. This is demonstrated in 1-D in Figure 1, where Ω^{H_k} is the macro element in the H_k-grid corresponding to node k while Ω^{P_k} is the corresponding patch of elements around node k in the h-grid. Note that $k = 1, 2, \ldots, n_{intr}$, where n_{intr} is the number of interior nodes in the h-grid. Therefore, there are n_{intr} grids at the H level, each of which is paired with the primary h-grid. This results in the following spaces for each interior node, $\boldsymbol{\mathcal{U}}^{H_k} \subset \boldsymbol{\mathcal{U}}^h \subset \boldsymbol{\mathcal{U}}$ and $\boldsymbol{\mathcal{V}}^{H_k} \subset \boldsymbol{\mathcal{V}}^h \subset \boldsymbol{\mathcal{V}}$, for the solution and weight functions, respectively.

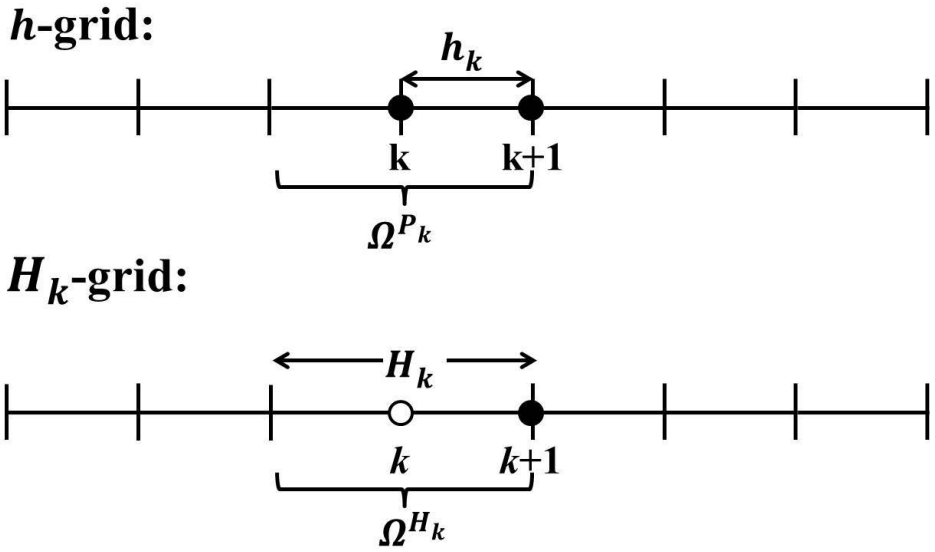

Figure 1: 1-D schematic of the h- and H-level grids for localized VGI

The local VGI procedure then uses the H_k-grids with the h-grid to compute the model parameter at every node k in the h-grid. By setting $\boldsymbol{W}^h = \boldsymbol{W}^{H_k}$, since $\boldsymbol{\mathcal{V}}^{H_k} \subset \boldsymbol{\mathcal{V}}^h \subset \boldsymbol{\mathcal{V}}$, we get (for details see [9])

$$\begin{aligned} M_{comb}(\boldsymbol{W}^{H_k}, \boldsymbol{U}^h; C_S^k, h_k) - M_{comb}(\boldsymbol{W}^{H_k}, \boldsymbol{U}^{H_k}; C_S^k, H_k) = \\ -(B(\boldsymbol{W}^{H_k}, \boldsymbol{U}^h) - B(\boldsymbol{W}^{H_k}, \boldsymbol{U}^{H_k})) \end{aligned} \tag{13}$$

We recognize that determining $\boldsymbol{U}^{H_k}$ for each interior node k involves a grid-level computation or projection (operations which involve looping over the elements of the H_k-grid). This is prohibitive and therefore, a surrogate is considered. $\boldsymbol{U}^{H_k}$ is approximated within the macro element using a volume-weighted average of $\boldsymbol{U}^h$ while outside of the macro element the solution is assumed to be the same between the two grid levels. This assumption further bypasses a grid-level computation. This assumption arises from the requirement on the variational multiscale (VMS) method to provide element-level localization and the desire to yield nodal exactness at element corners.[21] This leads to $\boldsymbol{U}^{H_k} \approx \widetilde{\boldsymbol{U}}^{H_k}|_{\Omega^{H_k}} = \mathbb{A}^{H_k}(\boldsymbol{U}^h)$, where $\mathbb{A}^{H_k}$ is the local averaging operator defined below. This choice is only feasible when the spatial derivatives exist on the weight function. Furthermore, instead of using $\widetilde{\boldsymbol{U}}^{H_k}$ to compute $\boldsymbol{S}^{H_k}$, $\boldsymbol{S}^{H_k}$ is also approximated within the macro element as $\widetilde{\boldsymbol{S}}^{H_k}|_{\Omega^{H_k}} \approx \mathbb{A}^{H_k}(\boldsymbol{S}^h)$.

$$\mathbb{A}^{H_k}(f^h) = \frac{1}{|\Omega^{P_k}|} \int\limits_{\Omega_e^h \in \Omega^{P_k}} f^h d\Omega_e^h \tag{14}$$

where $|\Omega^{P_k}|$ is the volume of the local patch and Ω_e^h indicates an element in the h-grid. Furthermore, among all of the terms in Equation (13) not involving the unknown model parameter, the non-linear convective term is found to be dominating.[8,9] We note that this assumption holds exactly in a spectral setting where all the bilinear terms cancel out between the H- and h-level grids due to the L_2 orthogonality of spectral modes.[22] The local VGI simplifies to

$$\begin{aligned} M_{smag}(\boldsymbol{W}^{H_k}, \boldsymbol{U}^h; C_S^k, h_k)_{\Omega^{P_k}} - M_{smag}(\boldsymbol{W}^{H_k}, \widetilde{\boldsymbol{U}}^{H_k}; C_S^k, H_k)_{\Omega^{H_k}} \approx \\ -(B_2(\boldsymbol{W}^{H_k}, \boldsymbol{U}^h)_{\Omega^{P_k}} - B_2(\boldsymbol{W}^{H_k}, \widetilde{\boldsymbol{U}}^{H_k})_{\Omega^{H_k}}) \end{aligned} \tag{15}$$

Now an appropriate choice for $\boldsymbol{W}^{H_k} \in \boldsymbol{\mathcal{V}}^{H_k}$ must be made. In a 1D setting, we select $\boldsymbol{W}^{H_k} = [w_i^{H_k}, 0]^T$ with $w_i^{H_k}$ such that it is linear along a spatial direction within the macro element and is constant or flat outside. Within the macro element, $w_i^{H_k}$ is selected such that

$$w_{i,j}^{H_k} = \frac{1}{\prod_{j=1}^{N} (H_k)_j} = \frac{1}{|\Omega^{H_k}|} \tag{16}$$

where $(H_k)_j$ is the element length along the j^{th} direction and $|\Omega^{H_k}|$ is the volume of the element. Such a choice of $\boldsymbol{W}^{H_k}$ is also feasible in a multi-D setting and on an unstructured mesh consisting elements of mixed topology, however, a larger patch must be considered. An extra layer of elements is needed around the macro element to attain a constant value in the outside region. This extra layer acts as a buffer region. This choice is made due to its ease of implementation. For more details see [8, 9].

II.B.2. Local VGI Computation

At this point we drop the subscript k in H_k and P_k and superscript k in C_S^k for brevity and only use it when necessary. The residual of the local VGI is defined as

$$\epsilon_{ij} = L_{ij} - 2(C_S h)^2 M_{ij} \tag{17}$$

where

$$L_{ij} = \left(\left(\frac{1}{|\Omega^H|}, u_i^h u_j^h \right)_{\Omega^P} - \left(\frac{1}{|\Omega^H|}, \widetilde{u}_i^H \widetilde{u}_j^H \right)_{\Omega^H} \right) \tag{18}$$

$$M_{ij} = \left(\left(\frac{1}{|\Omega^H|}, |S^h| S_{ij}^h \right)_{\Omega^P} - \left(\frac{H}{h} \right)^2 \left(\frac{1}{|\Omega^H|}, |\widetilde{S}^H| \widetilde{S}_{ij}^H \right)_{\Omega^H} \right) \tag{19}$$

The least squares method is applied to determine the model parameter as follows

$$(C_S h)^2 = \frac{1}{2} \frac{L_{ij} M_{ij}}{M_{ij} M_{ij}} \tag{20}$$

Since the local VGI procedure often leads to negative values for $(C_S h)^2$, an averaging scheme is employed to avoid this issue. Specifically, Lagrangian averaging is applied.[23] To do so, two additional advection-relaxation scalar equations are solved. These are shown in Equations (21) and (22). The scalars I_{LM} and I_{MM} in these equations are the Lagrangian-averaged counterparts of $L_{ij}M_{ij}$ and $M_{ij}M_{ij}$, respectively.

$$I_{LM,t} + (u_j - u_j^m) I_{LM,j} = \frac{1}{T}(L_{ij} M_{ij} - I_{LM}) \tag{21}$$

$$I_{MM,t} + (u_j - u_j^m) I_{MM,j} = \frac{1}{T}(M_{ij} M_{ij} - I_{MM}) \tag{22}$$

where T is the timescale over which averaging is applied. Additionally, a local volume-weighted averaging is also applied separately to the numerator and denominator of Equation (20) as follows

$$(C_S h)^2 = \frac{1}{2} \frac{\mathbb{A}^H(I_{LM})}{\mathbb{A}^H(I_{MM})} \tag{23}$$

where, as before, $\mathbb{A}^H$ represents a local averaging operator. This is equivalent to averaging over local pathtubes[8, 9] and maintains the utility of the local VGI.

III. Results and Discussion

III.A. Problem Setup and Discretization

The current work considers two sets of cases with surging airfoils at a fixed angle of attack (see Figure 2). In each set, the airfoil is subjected to a sinusoidal surging motion with streamwise oscillation at a fixed angle of attack and under a constant free-stream velocity. In one set, the amplitude of the oscillation is varied within a moderate range, while a high range is considered in the other set. For the moderate range, NACA 0018 airfoil at a mean Reynolds number of 300,000 and 4° angle of attack is considered at two advance ratios to match with the experiments of Strangfeld *et al.*[1] Mean Reynolds number is defined as $Re_C = U_\infty C/\nu$, where

U_∞ is the free-stream velocity and C is the chord of the airfoil. For advance ratios in the high range, NACA 0012 airfoil at a mean Reynolds number of 40,000 and 6° angle of attack is considered at three advance ratios to match with the experiments of Granlund *et al.*[2]

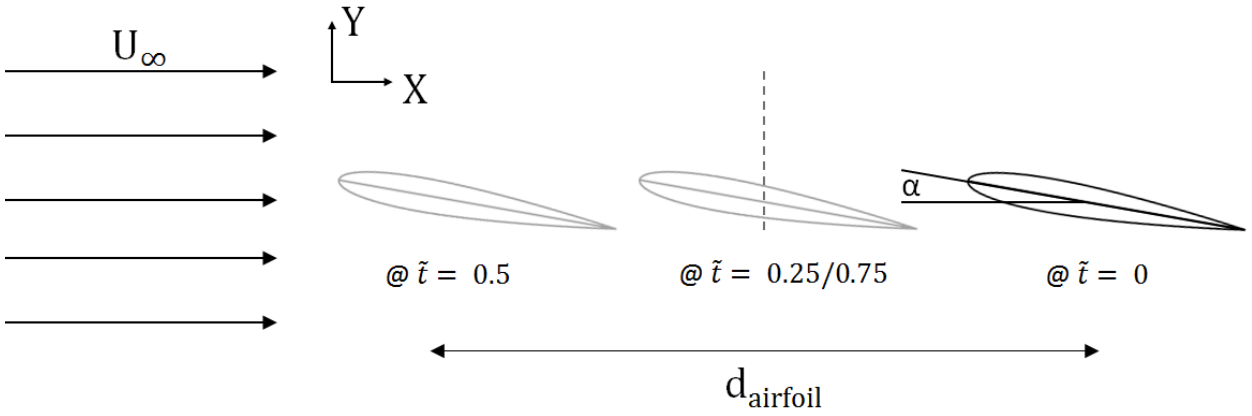

Figure 2: Schematic of the problem

As mentioned above, the airfoil is oscillated at a specified frequency (f) and amplitude (A) such that the displacement of the airfoil is given as

$$d_{airfoil} = Acos(2\pi ft) = Acos(2\pi t/T) = Acos(2\pi\tilde{t}) \tag{24}$$

where $T = 1/f$ is the time period. The variable $\tilde{t}$ is the fractional part in the oscillation cycle and is defined as $\tilde{t} = \{t/T\} = t/T - \lfloor t/T \rfloor$ (where $\lfloor\cdot\rfloor$ is the floor function). The reduced frequency is defined as $k = \pi fC/U_\infty$.

The amplitude of is defined as

$$A = \frac{\lambda c}{2k} \tag{25}$$

where λ is the advance ratio. The relative velocity is expressed as

$$U = U_\infty - U_{airfoil} = U_\infty(1 + \lambda sin(2\pi\tilde{t})) \tag{26}$$

At $\tilde{t}$=0 or ϕ=0° (where, ϕ denotes the phase in the cycle), the airfoil velocity is zero and thus, the relative velocity is the free-stream velocity and same holds at $\tilde{t}$=0.5 or ϕ=180°. At $\tilde{t}$=0.25 or ϕ=90° the airfoil is at the maximum relative velocity and at $\tilde{t}$=0.75 or ϕ=270° at the minimum relative velocity.

For the NACA 0018 airfoil, two advance ratios of λ=0.34 and 0.51 are investigated, while three advance ratios of λ=0.8, 1.0 and 1.2 are considered for the NACA 0012 airfoil. Note that the highest advance ratio case involves the reversed flow condition, where in a part of the surging cycle the relative flow becomes negative or is from the geometric trailing end of the airfoil to the leading end. Reduced frequency is set at 0.133 for the NACA 0012 airfoil for all three advance ratios while for the NACA 0018 airfoil it is set at 0.08 and 0.0985 for λ=0.34 and 0.51, respectively. A second-order implicit time integration scheme (e.g., see Tran and Sahni[9]) is employed with 2,500 steps in an oscillation cycle.

The computational domain is set to be $100C$ x $50C$ x $0.2C$. At the inlet, constant free-stream velocity is applied and the airfoil is moved in the streamwise direction to achieve the sinusoidally varying relative velocity. No-slip condition is prescribed on the airfoil surface, i.e., flow velocity on the airfoil surface is prescribed to match with the velocity of the airfoil. Slip condition is set at the top and bottom surfaces. Side surfaces are imposed to be periodic. A natural pressure condition is used at the outlet.

The mesh is comprised of an unstructured mixed mesh (with hex and wedge elements). An extrusion is applied in the spanwise direction. For the NACA 0018 airfoil case at $Re_C = 300,000$, 50 layers are used in the span while 25 layers are used for the case with NACA 0012 airfoil at $Re_C = 40,000$. A layered and graded mesh is used around the airfoil surface, see Figures 4a and 4b. The first layer height is set to be $\mathcal{O}(10^{-4}C)$ and a geometric growth is applied to about 20 layers with a growth rate of 1.2. Refinement zones are placed around the airfoil to resolve the flow structures of interest, see Figure 3 (where refinement zones

are noted). Note that a similar mesh is used for both the airfoils. Mesh statistics for both airfoil cases are listed in Table 1.

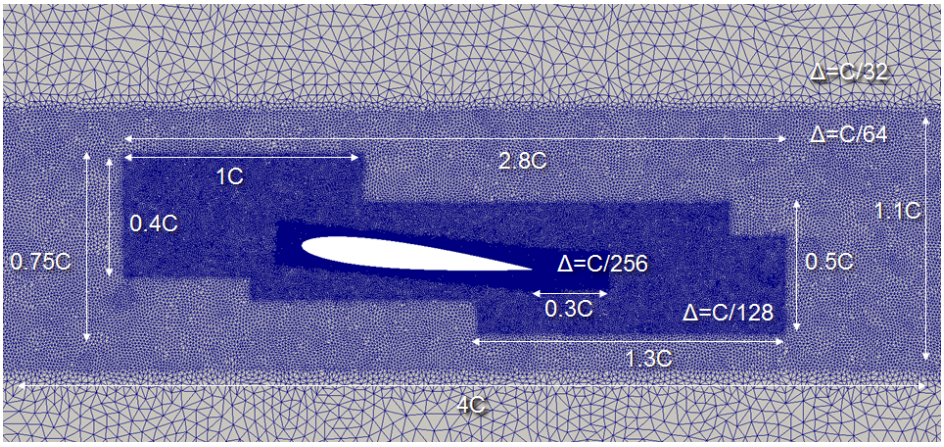

Figure 3: Mesh with refinement zones around the NACA 0012 airfoil (a similar mesh is used in the case with NACA 0018 airfoil)

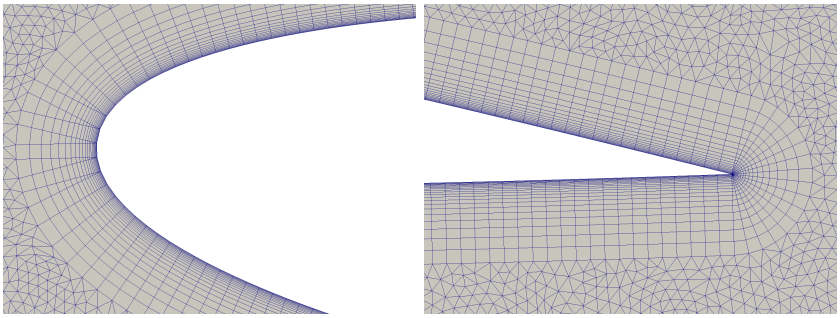

(a) Leading Edge (b) Trailing Edge

Figure 4: Layered and graded mesh around the NACA 0012 airfoil (a similar mesh is used in the case with NACA 0018 airfoil)

Table 1: Mesh statistics

Airfoil	# of nodes	# of elements
NACA 0018 (λ={0.34,0.51}, Re_C=300,000)	5,703,180	7,046,976
NACA 0012 (λ={0.8,1.0,1.2}, Re_C=40,000)	2,137,850	3,811,650

III.B. Moderate Advance Ratio

III.B.1. Force Response

Normalized lift (L/L_0, where L_0 is the lift of the static airfoil) is shown in Figure 5. In this figure, LES predictions are compared to the experimental data[1] for both advance ratios of λ=0.34 and 0.51. We further note that the LES data is instantaneous (i.e., taken over a single cycle) and therefore, exhibits fluctuations due to the presence of a turbulent flow over the airfoil; phase-averaged data from simulations will be considered in the future. LES is carried out for three oscillation cycles and data is presented from the third cycle.

As expected, a high lift is observed at $\tilde{t}$=0.25 when the relative velocity is at its maximum (i.e., at the advancing side) while the lift is about minimum at $\tilde{t}$=0.75 (i.e., at the retreating side). For both advance ratios, the overall temporal profile of the lift closely exhibits a sinusoidal variation. Overall a good agreement is observed between the current LES predictions and experimental data.

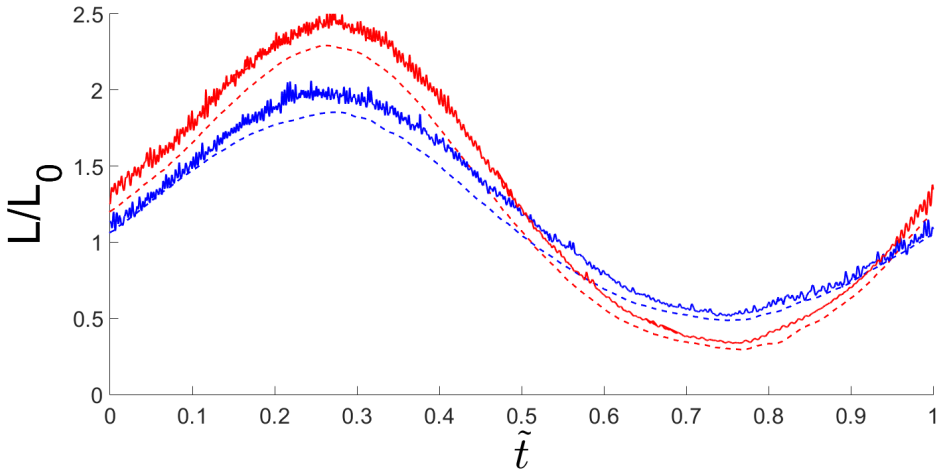

Figure 5: Normalized lift from LES (solid lines) and experiments[1] (dashed lines) for λ=0.34 (blue) and 0.51 (red)

III.B.2. Flowfields

Figure 6 shows instantaneous vorticity for both advance ratios at three phases in the cycle; relative velocity is shown at the top. The plots in this figure are with respect to the airfoil. Recall that at $\tilde{t}$=0 the relative velocity is at its mean value and entering into the advancing portion of the cycle while at $\tilde{t}$=0.25 and 0.75 it is at its maximum and minimum values, respectively. At any given phase, the flow pattern is similar between the two advance ratios. At $\tilde{t}$=0.25, the boundary layer is thinner as compared to other two phases (i.e., vorticity is confined much closer to the airfoil surface), as expected due to the maximum relative velocity and thus, a higher (instantaneous) Reynolds number. At $\tilde{t}$=0.75, vorticity accumulates around the airfoil due to deceleration of the airfoil until this phase and as a result wake is significantly different with less vortical structures as compared to the other two phases. Further, at this phase a marginal separation is seen on the pressure or lower side of the airfoil (again, due to airfoil deceleration).

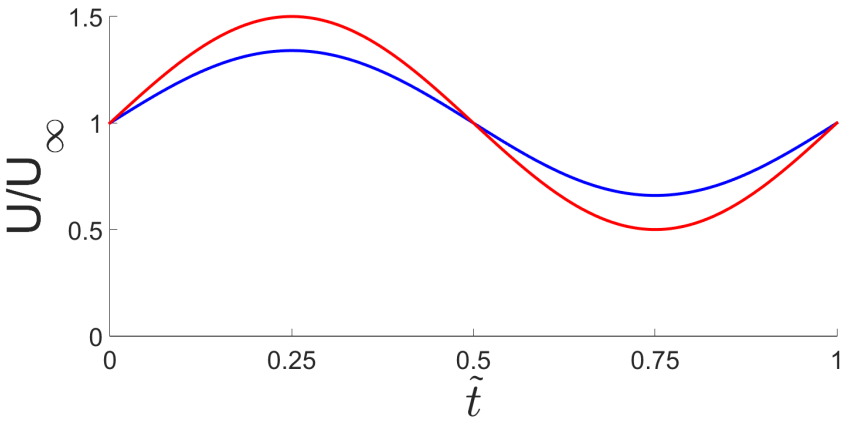

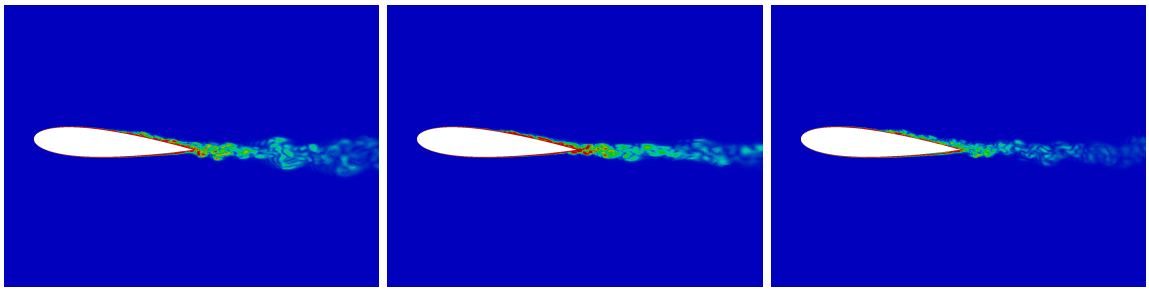

(a) $\lambda = 0.34$, $\tilde{t}$=0, $\phi = 0°$ (b) $\lambda = 0.34$, $\tilde{t}$=0.25, $\phi = 90°$ (c) $\lambda = 0.34$, $\tilde{t}$=0.75, $\phi = 270°$

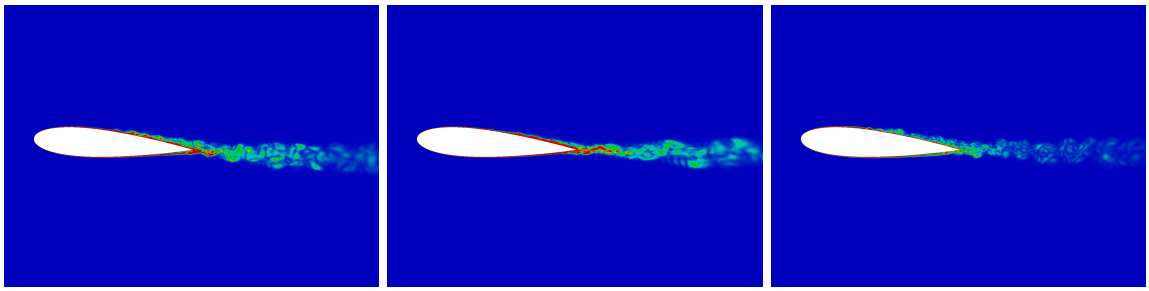

(d) $\lambda = 0.51$, $\tilde{t}$=0, $\phi = 0°$ (e) $\lambda = 0.51$, $\tilde{t}$=0.25, $\phi = 90°$ (f) $\lambda = 0.51$, $\tilde{t}$=0.75, $\phi = 270°$

Figure 6: Vorticity magnitude at three different phases for λ=0.34 and 0.51 (maximum value in the color range is set to $60U_\infty/C$); relative velocity is shown at the top for λ=0.34 (blue) and 0.51 (red)

III.C. High Advance Ratio

III.C.1. Force Response

Similar to the moderate advance ratio cases, normalized lift for the high advance ratio cases is shown in Figure 7. In this figure, LES predictions are compared to the experimental data[2] for three advance ratios of λ=0.8, 1.0 and 1.2. Similar to the previous case, LES data is instantaneous (i.e., taken over a single cycle) and therefore, exhibits fluctuations due to the presence of a turbulent flow over the airfoil; phase-averaged data from simulations will be considered in the future. For this case too, LES is carried out for three oscillation cycles and data is presented from the third cycle.

As before, a high lift is observed at $\tilde{t}$=0.25 when the relative velocity is at its maximum (i.e., at the advancing side) while while the lift is about minimum $\tilde{t}$=0.75 (i.e., at the retreating side). However, the lift is close to zero around $\tilde{t}$=0.75. For all three advance ratios, the overall temporal profile of the lift departs from a sinusoidal variation. Overall a good agreement is observed between the current LES predictions and experimental data.

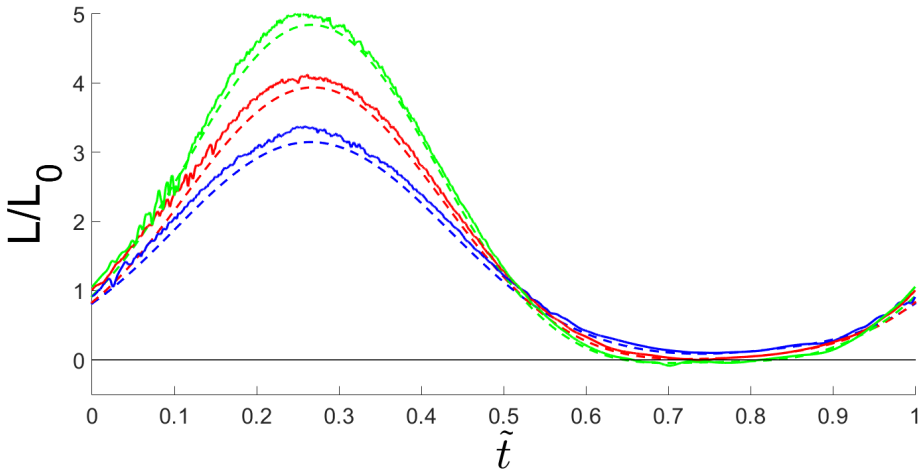

Figure 7: Normalized lift from LES (solid lines) and experiments[2] (dashed lines) for λ=0.8 (blue), 1.0 (red) and 1.2 (green)

III.C.2. Flowfields

Figure 8 shows instantaneous vorticity for all three advance ratios at three phases in the cycle; relative velocity is shown at the top. As before, the plots in this figure are with respect to the airfoil. Three phases are considered in retreating portion of the cycle, specifically $\tilde{t}$=0.55, 0.67 and 0.85 (or ϕ=198°, 241.2° and 306°). Recall that at $\tilde{t}$=0 the relative velocity is at its mean value and entering into the advancing portion of the cycle while at $\tilde{t}$=0.25 and 0.75 it is at its maximum and minimum values, respectively.

At $\tilde{t}$ = 0.55, see Figures 8a, 8d and 8g, the flow is fairly similar across all advance ratios. The flow is clearly turbulent and boundary layer is relatively thicker as compared to the moderate advance ratio cases shown in Figure 6 (i.e., due to a significant difference in the Reynolds number between the two sets of cases).

At $\tilde{t}$ = 0.67, a roll up of a distinct vortex is observed near the (geometric) leading edge on the suction or upper side of the airfoil; we refer to this vortex as the leading edge vortex (LEV). The position of LEV varies across the three advance ratios (see Figures 8b, 8e and 8h). In the case with λ = 0.8, the location of this vortex is furthest away from the (geometric) leading edge, while for λ = 1.2 it is closest to the leading edge. Note that this phase is just after the onset of flow reversal for λ = 1.2. Additionally, at this phase flow separation is observed on the pressure or lower side of the airfoil for each advance ratio.

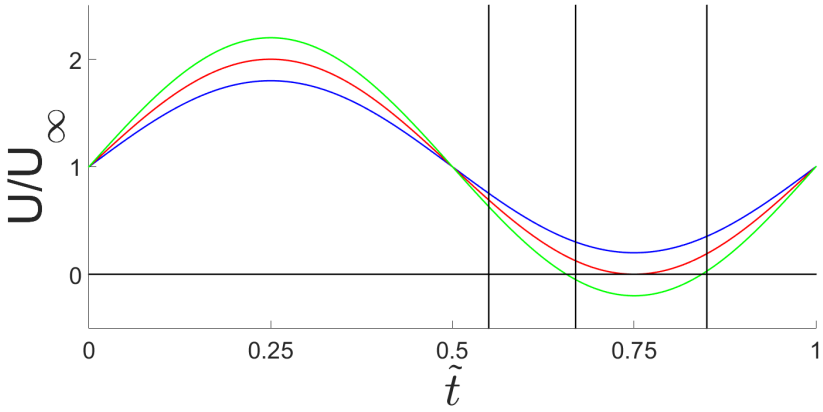

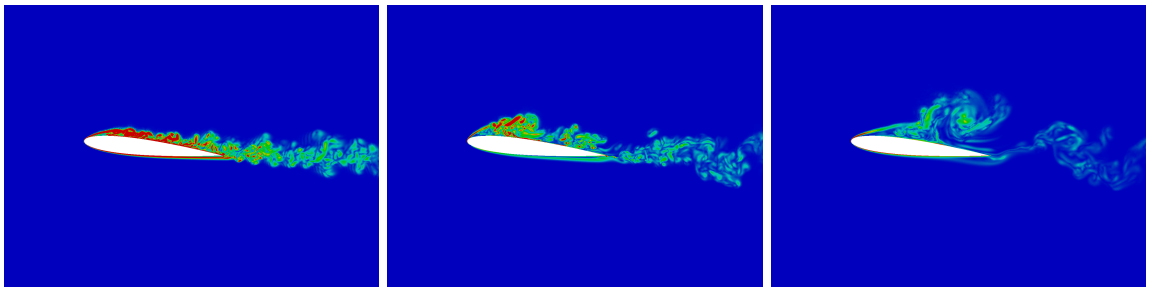

(a) $\lambda = 0.8$, $\tilde{t}$=0.55, $\phi = 198°$ (b) $\lambda = 0.8$, $\tilde{t}$=0.67, $\phi = 241.2°$ (c) $\lambda = 0.8$, $\tilde{t}$=0.85, $\phi = 306°$

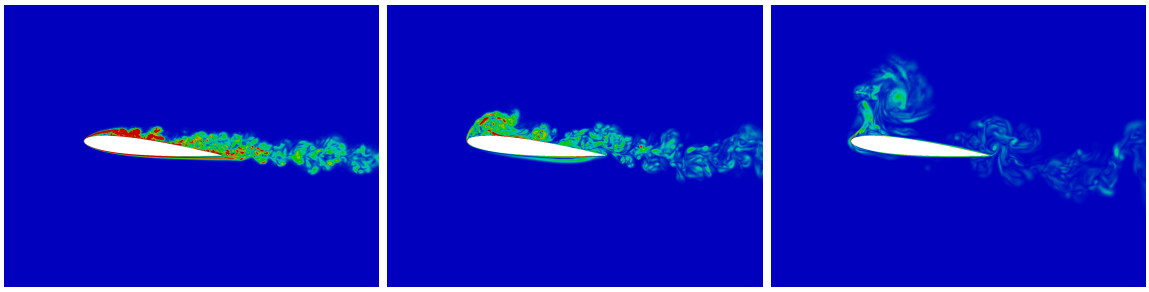

(d) $\lambda = 1.0$, $\tilde{t}$=0.55, $\phi = 198°$ (e) $\lambda = 1.0$, $\tilde{t}$=0.67, $\phi = 241.2°$ (f) $\lambda = 1.0$, $\tilde{t}$=0.85, $\phi = 306°$

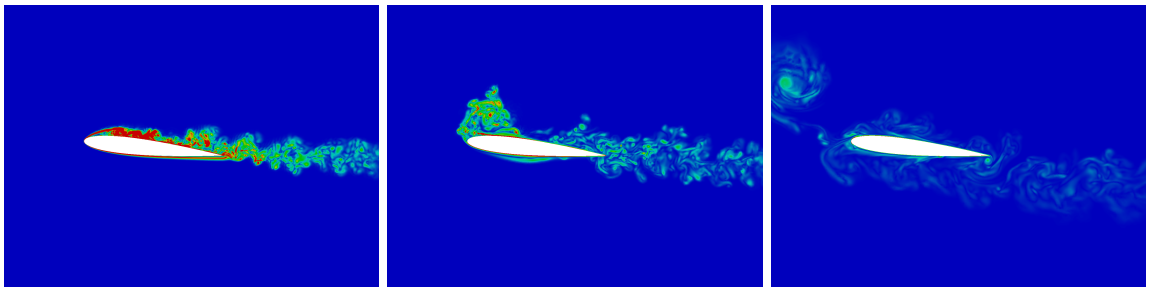

(g) $\lambda = 1.2$, $\tilde{t}$=0.55, $\phi = 198°$ (h) $\lambda = 1.2$, $\tilde{t}$=0.67, $\phi = 241.2°$ (i) $\lambda = 1.2$, $\tilde{t}$=0.85, $\phi = 306°$

Figure 8: Vorticity magnitude at three different phases for λ=0.8, 1.0 and 1.2 (maximum value in the color range is set to $40U_\infty/C$); relative velocity is shown at the top for λ=0.8 (blue), 1.0 (red) and 1.2 (green)

At $\tilde{t} = 0.85$, the relative velocity is increasing or recovering to its mean value. By this phase, the LEV is ejected or separates from the airfoil surface, see Figures 8c, 8f and 8i. For the case with $\lambda = 1.2$, the shed LEV is ahead of the (geometric) leading edge due to the presence of reverse flow regime (note that at $\tilde{t} = 0.85$ the flow reversal just ends for $\lambda = 1.2$). At this advance ratio and phase (see Figure 8i), a roll up of a secondary vortex is also seen at the (geometric) trailing edge on the pressure or lower side.

In Figure 9, evolution of the LEV is presented for each advance ratio. Images in the left column are at the

phase when the LEV is ejected or separates from the airfoil surface; this phase is different for each advance ratio. The middle column shows the LEV at $\tilde{t}$=0.75 or ϕ=270° which is the point of the minimum relative velocity. Note that for λ=0.8 LEV is ejected at $\tilde{t}$=0.75 or ϕ=270°. The right column is at the phase when the LEV reaches the (geometric) trailing edge of the airfoil (again, this phase is different for each advance ratio).

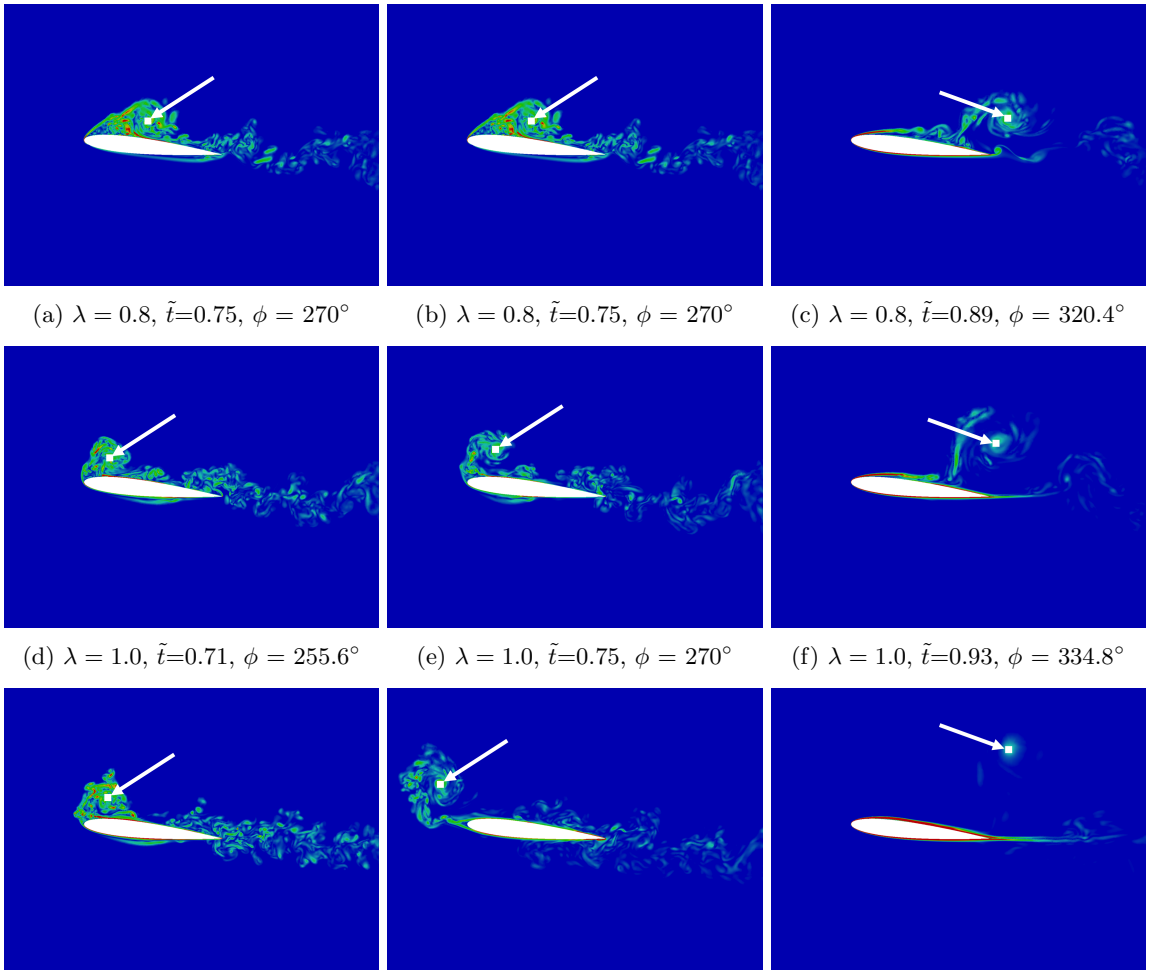

(a) $\lambda = 0.8$, $\tilde{t}$=0.75, $\phi = 270°$ (b) $\lambda = 0.8$, $\tilde{t}$=0.75, $\phi = 270°$ (c) $\lambda = 0.8$, $\tilde{t}$=0.89, $\phi = 320.4°$

(d) $\lambda = 1.0$, $\tilde{t}$=0.71, $\phi = 255.6°$ (e) $\lambda = 1.0$, $\tilde{t}$=0.75, $\phi = 270°$ (f) $\lambda = 1.0$, $\tilde{t}$=0.93, $\phi = 334.8°$

(g) $\lambda = 1.2$, $\tilde{t}$=0.67, $\phi = 241.2°$ (h) $\lambda = 1.2$, $\tilde{t}$=0.75, $\phi = 270°$ (i) $\lambda = 1.2$, $\tilde{t}$=0.99, $\phi = 356.4°$

Figure 9: LEV evolution for λ=0.8, 1.0 and 1.2 (in each image an arrow is used to indicate the LEV position)

The horizontal and vertical positions of the LEV is tracked for each advance ratio in the interval from when the LEV is ejected from the airfoil through when it passes the trailing edge. Figure 10 shows the tracking of LEV. The position at the ejection or separation phase is set to be zero and incremental position, or displacement, is shown for all later phases (i.e., $\Delta X_{LEV}/C$ and $\Delta Y_{LEV}/C$). As before, the ejection or separation phase is different for each curve corresponding to an advance ratio and therefore, each curve is shifted. The horizontal position follows a straight line for each advance ratio that is parallel between all three advance ratios. The slope of this line is roughly the free-stream velocity, i.e., the LEV is advected in the horizontal direction by roughly the free-stream velocity. The vertical position increases in the beginning and then reaches a maximum value or saturates by the end of the interval. This behavior is observed for each advance ratio, however, the maximum vertical position or displacement increases with the advance ratio.

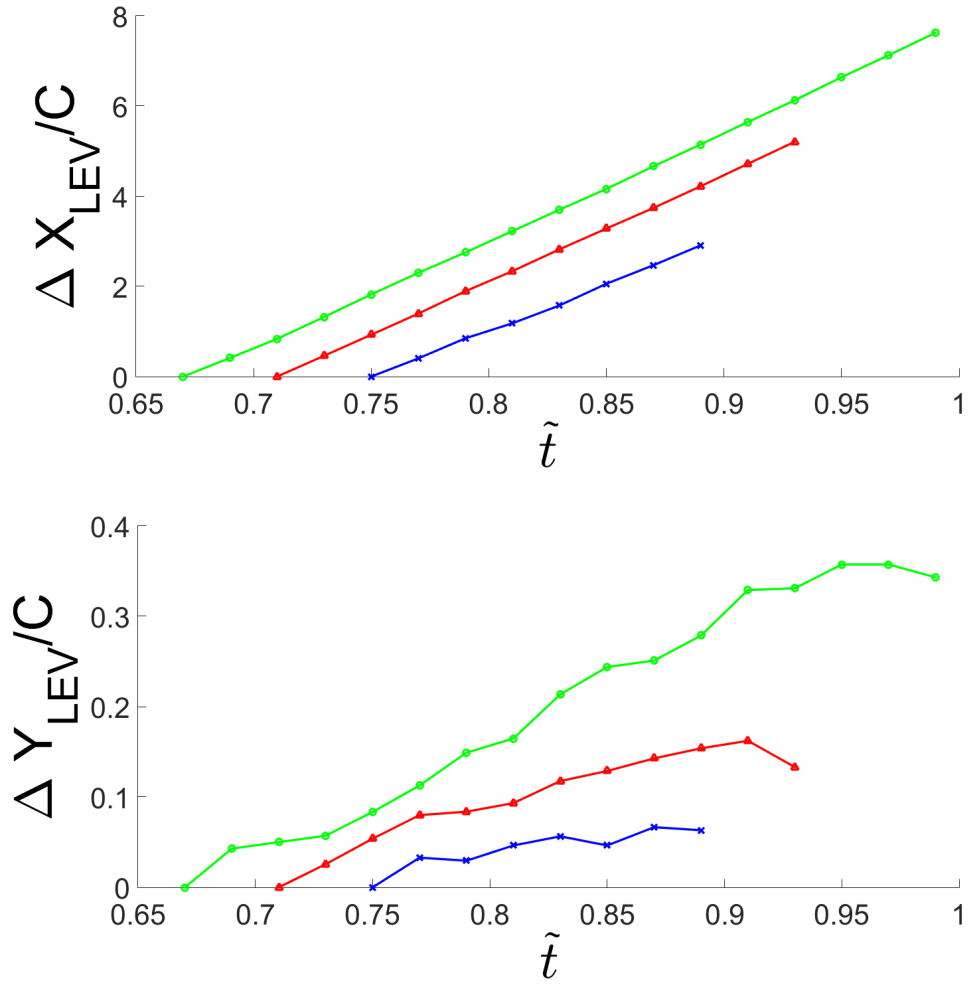

Figure 10: Horizontal (top) and vertical (bottom) positions of the LEV for λ=0.8 (blue), 1.0 (red) and 1.2 (green)

IV. Closing Remarks

A large eddy simulation (LES) based numerical investigation was carried out for flow over two surging airfoils with moderate to large streamwise oscillations. Two sets of cases were considered. In each set, the airfoil was subjected to a sinusoidal surging motion with streamwise oscillation at a fixed angle of attack. In one set, the amplitude of the oscillation was varied within a moderate range, while a high range was considered in the other set. For the moderate range, NACA 0018 airfoil at a mean Reynolds number of 300,000 and 4° angle of attack was considered. Two advance ratios of 0.34 and 0.51 were considered to match with the experiments of Strangfeld *et al.*[1] For the high range, NACA 0012 airfoil at a mean Reynolds number of 40,000 and 6° angle of attack was considered at three advance ratios of 0.8, 1.0 and 1.2 to match with the experiments of Granlund *et al.*[2] Note that the highest advance ratio case involves the reversed flow condition, where in a part of the surging cycle the relative flow becomes negative or is from the geometric trailing end of the airfoil to the leading end.

For each set, lift forces were compared between the experiments and simulations. Overall a good agreement is obtained for the lift force in all cases. Additionally, flowfields at different phases of the surge cycle are examined from simulations. For the moderate advance ratio cases, a similar flow pattern was observed between the two advance ratios and no distinct vortex was shed from the airfoil. On the other hand, in all three high advance ratio cases a distinct vortex was shed near the (geometric) leading edge on the suction or upper side. This prominent leading-edge vortex (LEV) was shed as the minimum velocity is reached in the

surging cycle and was advected downstream by roughly the free-stream velocity (in the horizontal direction). The relative position of the shed vortex (with respect to the airfoil) varied significantly between the three high advance ratio cases; it crossed the leading edge before sweeping over the airfoil in the case with the highest advance ratio of 1.2 (i.e., in the case with the reverse flow regime).

Acknowledgments

We would like to acknowledge that the computational resources used in this study were provided by Rensselaer's Center for Computational Innovations (CCI). We would also like to acknowledge that meshing software was provided by Simmetrix, Inc. This research was funded in part by National Science Foundation's CAREER grant 1350454 and by the Department of Energy, Office of Science's SciDAC-III Institute as part of the Frameworks, Algorithms, and Scalable Technologies for Mathematics (FASTMath) program under grant DE-SC0006617.

References

[1]Strangfeld, C., Müller-Vahl, H., Nayeri, C., Paschereit, C., and Greenblatt, D., "Airfoil in a high amplitude oscillating stream," *Journal of Fluid Mechanics*, Vol. 793, 2016, pp. 79–108.

[2]Granlund, K. O., Ol, M. V., and Jones, A. R., "Streamwise oscillation of airfoils into reverse flow," *AIAA Journal*, Vol. 54, No. 5, 2016, pp. 1628–1636.

[3]Greenblatt, D., Mueller-Vahl, H., Strangfeld, C., Ol, M. V., and Granlund, K. O., "High advance-ratio airfoil streamwise oscillations: wind tunnel vs. water tunnel," *54th AIAA Aerospace Sciences Meeting*, 2016, AIAA Paper 2016-1356.

[4]Visbal, M. R., "Analysis of the onset of dynamic stall using high-fidelity large-eddy simulations," *52nd Aerospace Sciences Meeting*, 2014, AIAA Paper 2016-0591.

[5]Hodara, J., Lind, A. H., Jones, A. R., and Smith, M. J., "Collaborative investigation of the aerodynamic behavior of airfoils in reverse flow," *Journal of the American Helicopter Society*, Vol. 61, No. 3, 2016, pp. 1–15.

[6]Norman, T. R., Shinoda, P., Peterson, R. L., and Datta, A., "Full-scale wind tunnel test of the UH-60A airloads rotor," *American Helicopter Society 67th Annual Forum*, 2011.

[7]Potsdam, M., Datta, A., and Jayaraman, B., "Computational investigation and fundamental understanding of a slowed UH-60A rotor at high advance ratios," *Journal of the American Helicopter Society*, Vol. 61, No. 2, 2016, pp. 1–17.

[8]Tran, S., Cummings, R., and Sahni, O., "Finite element based large eddy simulation of flow over bluff bodies," *Computers & Fluids*, (in print), `http://dx.doi.org/10.1016/j.compfluid.2016.10.027`.

[9]Tran, S. and Sahni, O., "Finite element based large eddy simulation using a combination of the variational multiscale method and the dynamic Smagorinsky model," *Journal of Turbulence*, (in print), `http://dx.doi.org/10.1080/14685248.2017.1280607`.

[10]Tran, S. and Sahni, O., "Large eddy simulation based on the residual-based variational multiscale method and Lagrangian dynamic Smagorinsky model," *54th AIAA Aerospace Sciences Meeting*, 2016, AIAA Paper 2016-0341.

[11]Cummings, R., Tran, S., and Sahni, O., "Finite element based large eddy simulation of a flow over an oscillating cylinder," *Proc. 8th International Colloquium on Bluff Body Aerodynamics and Applications*, 2016.

[12]Sahni, O., Jansen, K. E., Shephard, M. S., Taylor, C. A., and Beall, M. W., "Adaptive boundary layer meshing for viscous flow simulations," *Engineering with Computers*, Vol. 24, No. 3, 2008, pp. 267–285.

[13]Rodriguez, J. M., Sahni, O., Lahey, R. T., and Jansen, K. E., "A parallel adaptive mesh method for the numerical simulation of multiphase flows," *Computers & Fluids*, Vol. 87, 2013, pp. 115–131.

[14]Sahni, O., Ovcharenko, A., Chitale, K. C., Jansen, K. E., and Shephard, M. S., "Parallel anisotropic mesh adaptation with boundary layers for automated viscous flow simulations," *Engineering with Computers*, (in print), `http://dx.doi.org/10.1007/s00366-016-0437-2`.

[15]Sahni, O., Luo, X., Jansen, K., and Shephard, M., "Curved boundary layer meshing for adaptive viscous flow simulations," *Finite Elements in Analysis and Design*, Vol. 46, No. 1, 2010, pp. 132–139.

[16]Zhang, A. and Sahni, O., "Finite element analysis of boundary layer flows using a mixed B-spline setting on hybrid meshes," *54th AIAA Aerospace Sciences Meeting*, 2016, AIAA Paper 2016-1099.

[17]Sahni, O., Zhou, M., Shephard, M. S., and Jansen, K. E., "Scalable implicit finite element solver for massively parallel processing with demonstration to 160k cores," *Proceedings of the Conference on High Performance Computing Networking, Storage and Analysis*, 2009, pp. 1–12.

[18]Sahni, O., Carothers, C. D., Shephard, M. S., and Jansen, K. E., "Strong scaling analysis of a parallel, unstructured, implicit solver and the influence of the operating system interference," *Scientific Programming*, Vol. 17, No. 3, 2009, pp. 261–274.

[19]Zhou, M., Sahni, O., Kim, H. J., Figueroa, C. A., Taylor, C. A., Shephard, M. S., and Jansen, K. E., "Cardiovascular flow simulation at extreme scale," *Computational Mechanics*, Vol. 46, No. 1, 2010, pp. 71–82.

[20]Wang, Z. and Oberai, A. A., "A mixed large eddy simulation model based on the residual-based variational multiscale formulation," *Physics of Fluids*, Vol. 22, No. 7, 2010, pp. 075107.

[21]Hughes, T. J. and Sangalli, G., "Variational multiscale analysis: the fine-scale Green's function, projection, optimization, localization, and stabilized methods," *SIAM Journal on Numerical Analysis*, Vol. 45, No. 2, 2007, pp. 539–557.

[22]Oberai, A. and Wanderer, J., "Variational formulation of the Germano identity for the Navier-Stokes equations," *Journal of Turbulence*, Vol. 6, 2005, pp. N7.

[23]Meneveau, C., Lund, T. S., and Cabot, W. H., "A Lagrangian dynamic subgrid-scale model of turbulence," *Journal of Fluid Mechanics*, Vol. 319, 1996, pp. 353–385.